Chemical Science

ROYAL SOCIETY OF CHEMISTRY

EDGE ARTICLE

View Article Online
View Journal | View Issue

Cite this: *Chem. Sci.*, 2024, **15**, 3300

All publication charges for this article have been paid for by the Royal Society of Chemistry

Spin polarized electron dynamics enhance water splitting efficiency by yttrium iron garnet photoanodes: a new platform for spin selective photocatalysis†

Harshad Gajapathy,[a] Savini Bandaranayake,[a] Emily Hruska,[a] Aravind Vadakkayil,[b] Brian P. Bloom,[b] Stephen Londo,[a] Jackson McClellan,[a] Jason Guo,[c] Daniel Russell,[c] Frank M. F. de Groot,[d] Fengyuan Yang,[c] David H. Waldeck,[b] Martin Schultze[e] and L. Robert Baker *[a]

This work presents a spectroscopic and photocatalytic comparison of water splitting using yttrium iron garnet ($Y_3Fe_5O_{12}$, YIG) and hematite (α-Fe_2O_3) photoanodes. Despite similar electronic structures, YIG significantly outperforms widely studied hematite, displaying more than an order of magnitude increase in photocurrent density. Probing the charge and spin dynamics by ultrafast, surface-sensitive XUV spectroscopy reveals that the enhanced performance arises from (1) reduced polaron formation in YIG compared to hematite and (2) an intrinsic spin polarization of catalytic photocurrents in YIG. Ultrafast XUV measurements show a reduction in the formation of surface electron polarons compared to hematite due to site-dependent electron–phonon coupling. This leads to spin polarized photocurrents in YIG where efficient charge separation occurs on the T_d sub-lattice compared to fast trapping and electron/hole pair recombination on the O_h sub-lattice. These lattice-dependent dynamics result in a long-lived spin aligned hole population at the YIG surface, which is directly observed using XUV magnetic circular dichroism. Comparison of the Fe $M_{2,3}$ and O L_1-edges show that spin aligned holes are hybridized between O 2p and Fe 3d valence band states, and these holes are responsible for highly efficient, spin selective water oxidation by YIG. Together, these results point to YIG as a new platform for highly efficient, spin selective photocatalysis.

Received 13th June 2023
Accepted 16th January 2024

DOI: 10.1039/d3sc03016d

rsc.li/chemical-science

1. Introduction

Motivated by the need to identify stable, earth-abundant materials with optical and electronic properties that can be tailored for solar to chemical energy conversion, this work examines the carrier dynamics of two stable oxide semiconductors, yttrium iron garnet, and hematite, and correlates these properties with their water splitting efficiency. Photocatalytic water splitting on semiconductor electrodes offers a promising route to clean H_2 production.[1–4] This has the potential to facilitate a H_2 fuel economy[5,6] as well as reduce emissions from chemical processes requiring large quantities of H_2, such as the Haber–Bosch process[7,8] and Fischer–Tropsch[9,10] synthesis. While much effort has been devoted to understanding and controlling the redox potential and transport properties in candidate semiconductor photocatalysts, the role of electron spin is often overlooked when designing artificial photosynthetic systems.

In Nature, photosystem II performs water oxidation with remarkable efficiency using sunlight as the only energy source.[11,12] While a number of artificial devices have been demonstrated with photosynthetic efficiencies comparable to natural systems, most of these are ultimately limited by the stability, selectivity, or cost of the catalyst responsible for the water oxidation half-reaction. Notably, biological photosynthesis operates in chiral environments, and it has been proposed that this feature can promote efficiency because of the inherent spin selectivity of chiral matter.[13–16] This supposition is supported by theoretical studies which suggest that the $CaMn_4O_5$ cofactor of photosystem II acts as a spin control for enhancing water oxidation[17] and by studies that extend the

[a]*Department of Chemistry and Biochemistry, The Ohio State University, Columbus, Ohio 43210, USA. E-mail: baker.2364@osu.edu*

[b]*Department of Chemistry, University of Pittsburgh, 15260 Pittsburgh, Pennsylvania, USA*

[c]*Department of Physics, The Ohio State University, Columbus, Ohio 43210, USA*

[d]*Inorganic Chemistry and Catalysis, Debye Institute for Nanomaterials Science, Utrecht University, 3584CG Utrecht, The Netherlands*

[e]*Institute of Experimental Physics, Graz University of Technology, Petersgasse 16, Graz 8010, Austria*

† Electronic supplementary information (ESI) available. See DOI: https://doi.org/10.1039/d3sc03016d

principal of spin polarized enhanced water oxidation to artificial systems. For instance, chiral metal oxides have been shown to act as spin filters and result in spin selective photocatalysis, which reduces the reaction overpotential and increases the faradaic efficiency of the reaction.[18–25] Because O_2 forms on a triplet potential energy surface, spin selective photocatalysis can guide the reaction towards a triplet product and increase the kinetics of O_2 generation.[26–28]

Despite the application of chiral oxides for photocatalytic water splitting, the concept of spin polarized photocatalysis has yet to be evaluated for achiral magnetic semiconductors in which spin polarization results from magnetic exchange interactions rather than structural chirality. For electrocatalytic water oxidation in the dark, a number of studies have demonstrated that certain magnetic oxides display enhanced efficiency, presumably because of spin polarized transport within aligned domains of a magnetized anode.[29–33] Extending this approach to photocatalysis requires a combined understanding of the ground and excited state magnetic structure as well as the underlying photophysics that controls the spin states of transient, photoexcited redox carriers. To date, most spectroscopic studies have focused on studying spin polarized photoemission through a chiral layer[34–39] rather than spin accumulation at a catalyst surface, even though the latter is primarily responsible for driving spin selective catalysis. Owing to the challenge of spin selective spectroscopy with chemical state specificity and surface or interface sensitivity, the photoinduced spin polarization of a catalyst surface has not been directly observed for either a chiral or magnetic system.[40]

Although YIG is widely employed as a magnetic insulator in spintronic devices, it is not often used as a photocatalyst. One exception is a recent combinatorial synthesis of approximately 30 complex oxides that identified YIG as a promising photoanode for water oxidation.[41] On the other hand, hematite has been extensively explored as a photoanode for water solar splitting because of its ideal band gap, strong solar absorption, high chemical stability, and well-aligned band edge potential relative to the water oxidation half-reaction. In addition, Fe is one of the most abundant elements, making hematite almost universally accessible at a negligible cost. Despite these advantages, the photocatalytic efficiency of hematite remains low because of its poor electron carrier mobility, which is related to the efficient formation of small electron polarons that act as deep trap states.[42–46] Significantly improving electron transport in Fe oxide-based semiconductors could have a transformative effect on the field of solar fuels.

Using femtosecond time-resolved surface-sensitive Extreme Ultraviolet (XUV) spectroscopy, we directly compare the polaron formation efficiency in YIG to that in hematite and find that polaron formation in YIG is significantly reduced compared to hematite. A comparison of water oxidation by these two materials in the dark and under illumination confirms that YIG displays an 8-fold enhancement in photocurrent over hematite at a fixed potential of 2.0 V *vs.* RHE. This dramatic enhancement of photocatalytic activity also correlates with a significantly improved O_2 yield as quantified by rotating ring-disk measurements at pH 8. Finally, we confirm that the enhanced activity by YIG is a direct result of spin polarized photocurrents. To demonstrate this, we employ surface-sensitive XUV magnetic circular dichroism to directly observe the accumulation of spin aligned charge carriers at the photocatalyst surface under illumination. These measurements can directly probe the magnetic states of Fe in the thin film using the difference in $M_{2,3}$-edge absorption of Fe due to the polarization of light.[47–50] These XUV dichroism measurements at the Fe $M_{2,3}$-edge and the O L_1-edge reveal that spin aligned holes accumulate in the hybridized O 2p/Fe 3d valence band giving rise to spin polarized Fe^{4+} redox-active states in the O_h sublattice of YIG. Together, these results provide a detailed understanding of dramatically enhanced water splitting efficiency using a spin selective metal oxide photocatalyst and open the door for probing the effects of spin polarized currents in photosynthetic systems based on earth-abundant chiral and magnetic oxides.

2. Results and discussion

Fig. 1(a) shows the ground state static absorption spectrum of YIG and hematite. They both show an absorption feature with the peak centered at 55 eV. This feature corresponds to the 3p to 3d electronic excitation in Fe^{3+} atoms by the XUV probe. Because YIG and hematite contain Fe^{3+}, they share the same $M_{2,3}$-edge absorption peak. Despite subtle differences in lineshape between hematite, which contains only O_h Fe^{3+} centers, and YIG, which contains both O_h and T_d centers, it is not possible to cleanly resolve the O_h and T_d Fe^{3+} contributions due to strong overlap in the linear XUV spectrum. As we show below, however, these sites can be resolved using XUV magnetic circular dichroism owing to the opposite spin alignment of the O_h and T_d sub-lattices in YIG.

Although the ground state Fe $M_{2,3}$-edge of YIG and hematite are similar, they display very different responses in the ultrafast transient XUV measurements. Pumping with a 400 nm (3.1 eV) light pulse induces above bandgap excitation in both YIG (2.6–2.8 eV bandgap)[51,52] and hematite (2.0–2.2 eV bandgap).[53,54] The upper valence band of these materials comprises primarily O 2p orbitals and the conduction band comprises primarily Fe 3p orbitals[54,55] so that an above bandgap excitation constitutes an electron transfer from O to Fe atoms.[56] This charge transfer reduces Fe^{3+} atoms to Fe^{2+} and causes decrease in the $M_{2,3}$-edge absorption of Fe^{3+} which manifests as a bleach feature at 55 eV. Fig. 1(b) compares the transient XUV spectrum of YIG and hematite at 100 fs following photoexcitation, but before the relaxation of the photoexcited electron has occurred. As shown, both spectra display the characteristic bleach feature associated with a free conduction band electron in Fe 3d states.[44,45]

Following photoexcitation, the excited electrons in the Fe atoms of hematite couple with optical phonons to form a small electron polaron.[42,44–46] It has been shown previously that this trapped electron–polaron has an XUV spectral signature at the Fe $M_{2,3}$-edge around 52 eV.[57] Fig. 1(c) compares the transient spectra for YIG and hematite at 1 ps after photoexcitation following polaron formation. These data show that the polaronic yield is significantly reduced in the YIG as compared to hematite; *i.e.*, the absorbance at 52 eV is weaker for a similar

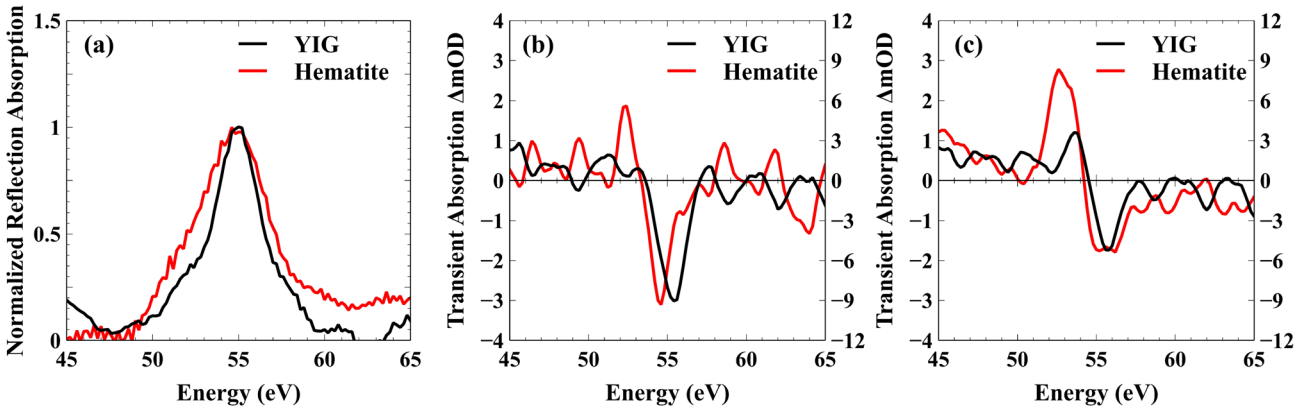

Fig. 1 Results of XUV-RA experiments on YIG (black) and hematite (red). (a) Ground state static absorption spectrum. (b) Transient absorption spectrum at 100 fs time delay between pump and probe. (c) Transient absorption spectrum at 1 ps time delay between pump and probe.

amount of bleach signal at 55 eV. Because hematite contains Fe atoms exclusively in O_h lattice sites whereas YIG contains Fe atoms in both T_d and O_h lattice sites (see Fig. 2(a)), one possible explanation for reduced polaron efficiency in YIG is that the electrons excited to the O_h Fe^{3+} centers strongly couple to optical phonons, while the electrons in the T_d Fe^{3+} are less susceptible to polaron formation. Because the excited electron in the O_h sub-lattice is localized in the low energy t_{2g} orbital compared to an e orbital for the T_d sub-lattice, this hypothesis is consistent with theoretical predictions that t_{2g} electrons have a stronger electron–phonon coupling and higher efficiency of small polaron formation than the e electrons.[58]

Note that YIG is a ferrimagnet with T_d and O_h electrons having opposite spins due to an antiferromagnetic coupling. In both lattice sites, Fe^{3+} atoms are in a high spin state with a $3d^5$ electronic configuration. By Pauli exclusion, the electrons excited by the pump pulse from the O 2p valence band into the Fe 3d conduction band must have a spin opposite to the already occupied Fe 3d electrons. Consequently, the conduction band electrons photoexcited to the T_d and O_h lattice sites must have opposite spins. From the transient XUV measurement, we hypothesize that the small polaron formation occurs only to the electrons in the O_h lattice sites in YIG. These trapped electrons have opposite spin relative to the electrons in the T_d lattice sites which do not form a polaron. Therefore, the polaronic electron trapping in the case of YIG is spin dependent. This indicates that electron transport in YIG is likely spin polarized because spin aligned electrons in the T_d lattice are significantly more mobile compared to electrons having the opposite spin, which form self-trapped, small electron polarons in the O_h lattice. As YIG is an n-type semiconductor, the surface bands have higher energy compared to the bulk. Accordingly, the non-trapped conduction electrons of one particular spin in the T_d sub-lattice are free to move from surface to bulk,[59] while the other spin electrons remain trapped as small polarons in the O_h sub-lattice (see Fig. 2(b) for a summary of the spin dependent electron transport). We note that the XUV spectra showing reduced polaron formation in YIG are consistent with reported conductivity measurements,[60–64] which measure the mobility of electrons in YIG to be within the range of 0.1 to 0.5 $cm^2\ V^{-1}\ s^{-1}$ whereas the mobility of electrons in hematite is reported to be on the order of 10^{-2} $cm^2\ V^{-1}\ s^{-1}$. The one-order of magnitude

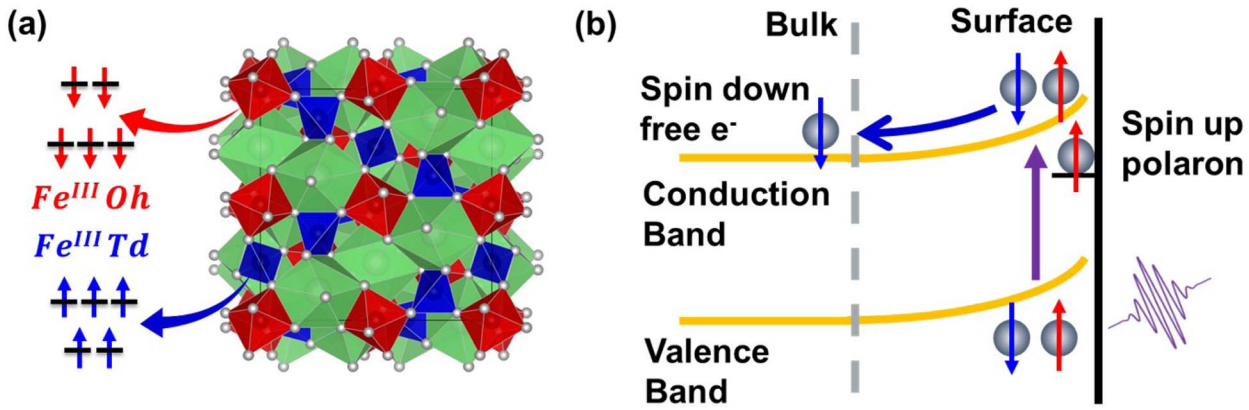

Fig. 2 (a) Crystal structure of YIG showing the Fe^{3+} atoms in T_d (blue) and O_h (red) lattice sites with opposite spins. (b) Illustrated band structure for YIG depicting how the interface potential leads to the drift of electrons to bulk and holes to the surface. Selective polaron formation in the O_h sub-lattice leads to spin selective trapping, which is expected to spin polarize the photoinduced current.

higher electron mobility in YIG compared to hematite can be attributed to reduced electron trapping in YIG due to the resistance of T_d electrons to form small polarons. These measurements are consistent with previous reports of electron transport in YIG based on a large polaron hopping model;[60,65,66] therefore, it is likely that the electrons excited to the T_d atoms form a large polaron.

To demonstrate the influence of ultrafast polaron formation on photocatalytic water splitting efficiency, Pastor *et al.* used photocurrent measured during *in situ* water oxidation as a direct readout for a pump–push experiment, where a visible pump pulse excites the hematite bandgap, a sub-picosecond delay allows time for polaron formation, followed by an IR push pulse to de-trap the electron.[42] This experiment reported a photocurrent enhancement by the IR pump pulse at the exact time constant measured for surface polaron formation by XUV reflection–absorption.[44,46] These results confirm that the formation of polarons in hematite actively limits water oxidation efficiency by hindering the removal of majority carriers from the depletion region resulting in eventual charge carrier recombination and loss of photoactive holes.[67–70] Consistent with the XUV measurements, we find that YIG displays nearly an order of magnitude higher photocurrent density for water oxidation relative to hematite. This can be observed in Fig. 3, which shows the current density of hematite (panel a) and YIG (panel b) with and without illumination. While dark currents are similar between these two materials, the light-driven photocatalytic response is significantly higher in YIG. Fig. 3(c) plots the difference between the total current in light and dark. At 2.15 V *vs.* RHE, YIG produces a 15-fold photocurrent enhancement relative to hematite increasing from 0.4 to 6.3 mA cm^{-2} at an illumination intensity of 100 mW cm^{-2}.

While the enhanced activity of YIG over hematite can be attributed in part to reduced polaron formation and greater electron mobility, below we show that the spin polarization of the photocurrent is also important. Photoexcitation of conduction band electrons leaves behind holes in the valence band. The electrons that trap as small polarons eventually recombine with their corresponding holes at a long time, circa 350–500 ps.[45,71] Before recombination, these holes can act as an electron acceptor at the anode during water oxidation. Assuming the conducting electrons in YIG are spin polarized, the holes left behind must be spin polarized as well. Because molecular O_2 has a triplet ground state, compared to singlet water, spin is not a conserved quantity during the O_2 evolution reaction (OER) when considering only the reactants. However, considering the spin of the redox active holes, which drive water oxidation, spin polarized currents show enhanced activity toward O_2 production since the transfer of two spin aligned holes balances the angular momentum of the triplet product. Consequently, spin polarized photocurrents may also play an important role in improving the efficiency of water oxidation.

To illustrate the significantly enhanced efficiency for O_2 evolution along the triplet reaction pathway by YIG compared to hematite, Fig. 4(a) shows the partial current density, the part of the total current density responsible for O_2 generation as measured using a rotating ring disk electrode. The O_2 partial current from the bare magnetic substrate is low indicating that negligible amounts of O_2 are produced in the absence of either the hematite or YIG catalyst. Hematite produces more O_2 than

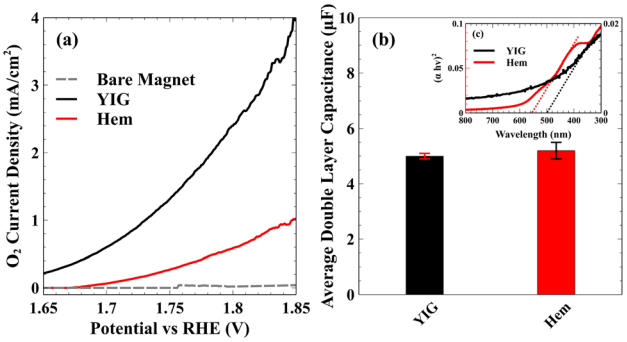

Fig. 4 (a) O_2 partial current density for bare magnetic electrode, hematite and YIG. (b) Double layer capacitance for YIG and hematite catalysts. (c) Tauc plots showing UV-Vis absorption by YIG and hematite catalysts confirming band gaps of 2.5 eV and 2.2 eV, respectively.

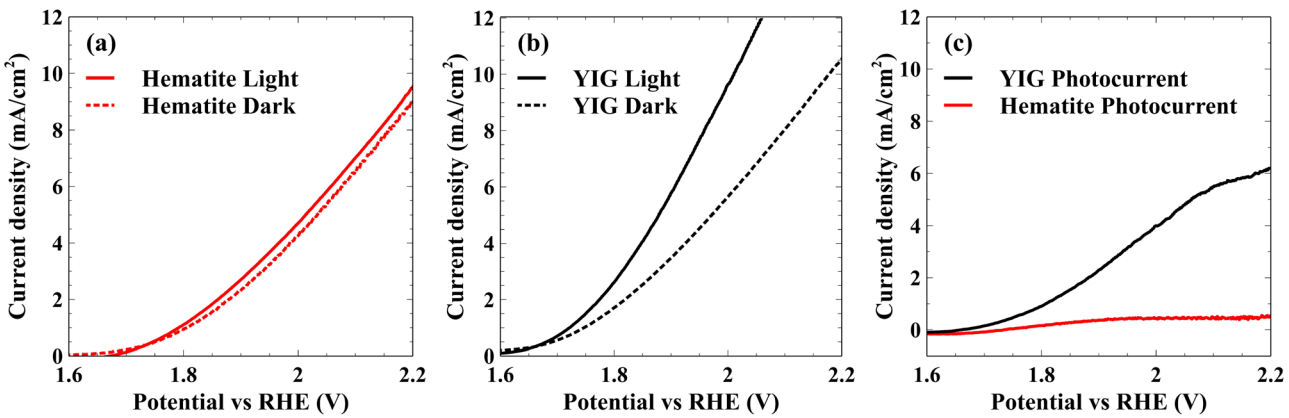

Fig. 3 Linear sweep voltammograms for hematite (a) and YIG (b) catalyst-loaded electrodes in the dark and upon irradiation. (c) Difference between dark and light current densities.

the bare magnetic electrode, but YIG has the highest performance among the three electrodes. O_2 partial current is only reported up to 1.85 V *vs.* RHE because bubble formation interferes with O_2 detection by the ring electrode at higher current densities. This significant enhancement in O_2 generation efficiency by YIG cannot be explained simply due to the difference in active area between hematite and YIG. To illustrate this, Fig. 4(b) shows a similar electrochemically active surface area for both YIG and hematite. Fig. 4(c) (inset) also shows that despite having lower absorbance and a slightly higher band gap than hematite, YIG still displays significantly enhanced photocurrent. Note that the data in Fig. 3 and 4 were obtained under a constant magnetic field, with a field strength high enough to saturate the out-of-plane magnetization of YIG and to ensure spin alignment of the respective sub-lattices across domains in the polycrystalline catalyst. Fig. S6 (see ESI†) shows the photocurrent without magnetization using a glassy carbon electrode. By comparison, the measurements using glassy carbon electrodes do not show such enhancement in YIG relative to hematite. Thus, the enhanced activity of YIG towards O_2 evolution under magnetization indicates that spin polarization plays a crucial role in the high performance of YIG.

While spin polarized currents have been predicted to explain enhanced efficiency for a variety of chiral and magnetic catalysts,[13,20,34,72–75] it has remained a significant challenge to visualize the actual spin accumulation at the catalyst surface. In this study, we show that surface-sensitive XUV Magnetic Circular Dichroism (MCD) is able to directly detect the spin polarized holes that drive spin selective OER. Here, the MCD signal is defined by the difference in absorption of circularly polarized light under the different sample magnetizations as described below. Fig. 5(a) depicts the excitation of the different spin states by the circularly polarized XUV light. As illustrated by the diagram, the magnetic field selectively stabilizes one sub-lattice in the sample while destabilizing the other, and electrons in the stabilized sub-lattice absorb at a different photon energy compared to the destabilized spins. Fig. 5(b) shows the MCD spectrum of YIG taken at the Fe $M_{2,3}$-edge. Ligand field multiplet simulations of the MCD spectrum were performed using the software package CTM4XAS (see ESI Section 3†).[76–79] Here the black line represents the experimental MCD spectrum, the grey line represents the simulated spectrum, and blue and red dashed lines represent individual contributions from the Fe^{3+} T_d and Fe^{3+} O_h sub-lattices, respectively. As shown, combined simulations of the T_d and O_h lattice sites in YIG closely reproduce the measured experimental spectrum.[77] Because these sub-lattices are aligned by the external magnetic field with opposite spins, the line shapes of the T_d and O_h contributions to the total MCD spectrum are opposite. Fig. 5(b) shows the ground state MCD spectrum and defines the initial state of YIG.

When illuminated with visible light the spectral features change because of the light-induced charge transfer from O 2p valence band states to Fe 3d conduction band states. To observe this effect on interfacial spin polarization, we employed a 400 nm pump pulse and broadband, circularly polarized XUV probe pulse each at a 1 kHz frequency. This experimental design means that if the relative pump–probe time delay is such that the probe pulse arrives at the sample before the pump pulse by a few ps, then the time delay between a pump pulse and the subsequent probe is approximately 1 ms defined by the laser repetition rate. As the probe–pump–probe–pump train arrives at the sample with a 1 kHz repetition rate, if the sample doesn't

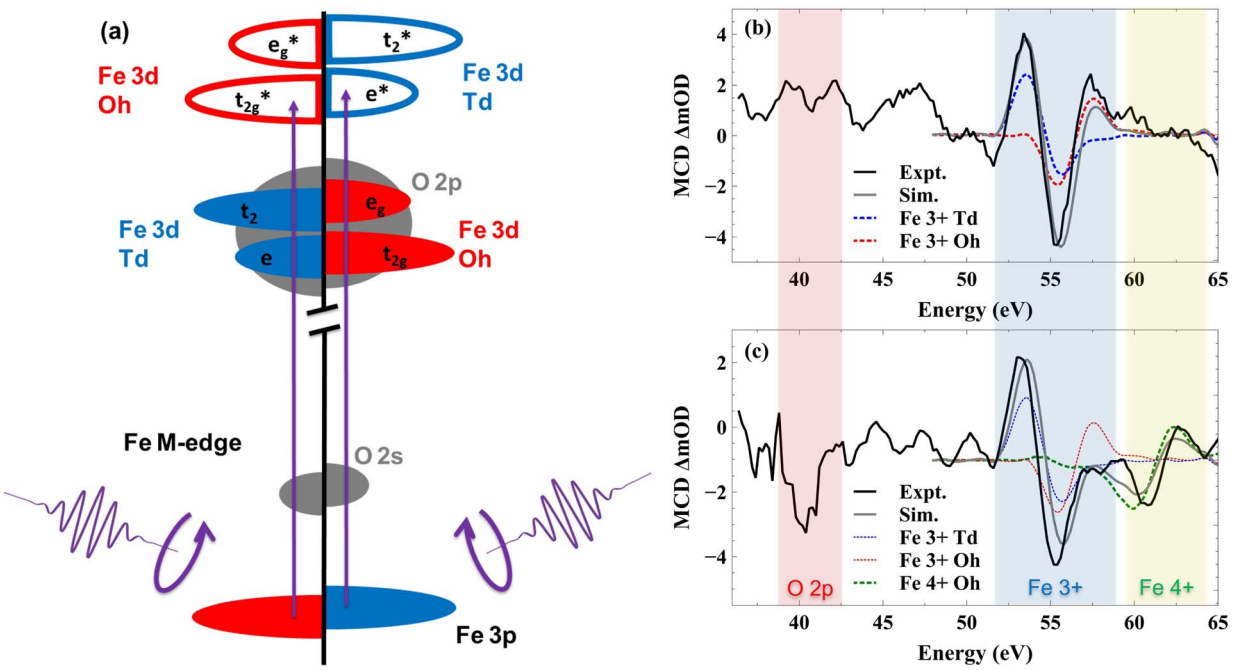

Fig. 5 (a) Illustrated band structure of YIG and associated XUV-MCD absorption at the Fe $M_{2,3}$-edge. (b) and (c) Comparison of experimental and simulated XUV-MCD spectra measured in the dark (b) and during illumination with a 1 kHz, 400 nm excitation beam (c).

return to its ground state in 1 ms, we can probe the corresponding long-lived excited state spectrum using the probe. Measuring the XUV-MCD spectrum under these conditions enables observation of long-lived spin polarized charge accumulation at the YIG surface. Any pump-induced changes to the MCD spectrum under these conditions represent spin polarized carriers having a sufficient lifetime to influence photocatalytic processes such as water oxidation.

The MCD spectrum of YIG under 400 nm illumination using this 1 ms time delay between pump and probe is shown in Fig. 5(c). There are two light-induced changes to the YIG spectrum resulting from 400 nm illumination. First, we observe a sharp dip at 40 eV. This feature is well below the Fe $M_{2,3}$-edge and matches previous reports of XUV absorption at the O L_1-edge corresponding to an O 2s to 2p transition.[56,78,79] Second, we observe a change in the Fe $M_{2,3}$-edge line shape with the loss of intensity at 58 eV and the appearance of a new feature at 60 eV. Considering first the O L_1-edge, no MCD signal is discernible in the ground state O L_1-edge spectrum. This observation is consistent with a full $2p^6$ electron configuration in Fe_2O_3, where Fe metal centers are in a 3+ oxidation state and O ligands are in a 2- oxidation state. The completely paired $2p^6$ electron configuration precludes any O contribution to ground-state magnetization. However, surface band bending in n-type YIG can drive holes to accumulate at the surface following photoexcitation. These holes are expected to have significant O 2p character, giving rise to unpaired electrons in the O 2p valence band. Accumulation of surface holes will only be detected in an MCD measurement to the extent that they display a net spin polarization. Consequently, the appearance of this spectral signature at the O L_1-edge upon illumination represents the direct detection of spin aligned holes in O 2p valence band states. The reason that the MCD signal at the O L_1-edge appears as a single negative dip rather than a peak and a dip similar to the various contributions to the Fe $M_{2,3}$-edge is consistent with a spin aligned hole in an O $2p^5$ electron configuration as described in the ESI Section 4.†

Because the valence band of YIG also includes contributions from Fe 3d orbitals, hybridization of the O 2p ligand hole with Fe 3d states is expected.[80] Previously, we showed that the position of the O L_1-edge absorption reflects the extent of O 2p and metal 3d valence band hybridization, with a redshift corresponding to a more strongly hybridized valence band.[56] Here the O L_1-edge feature appears at 40 eV, which is several eV redshifted compared to previous reports of photoexcited holes in Fe_2O_3, Co_3O_4, and NiO, suggesting that YIG shows greater metal–oxygen bond covalency compared to hematite and that the photoexcited holes should have both O 2p and Fe 3d character. This is consistent with previous reports that identify a combination of O 2p ligand holes[81–95] and high valent 4+ Fe[96–101] as the primary redox active states for water splitting in a variety of metal oxide catalysts.

The mixing of the ligand hole with Fe 3d states is evident in Fe $M_{2,3}$-edge MCD spectrum above 60 eV. These changes to the Fe $M_{2,3}$-edge MCD spectrum can be reproduced by including a contribution from Fe^{4+} O_h centers in the ligand field multiplet simulation. This new contribution is shown as the green dashed line in Fig. 5(c). The incorporation of a Fe^{4+} hole on the T_d sublattice is unable to reproduce the measured, excited state MCD signal (see ESI Section 3†). Consequently, we conclude that the spin polarized hole primarily hybridizes between O 2p and O_h Fe 3d states. This is equivalent to stating that the unpaired electrons generated by the creation of a valence band hole are ferromagnetically coupled to the Fe T_d sub-lattice, which is consistent with this sub-lattice controlling the net magnetic moment in YIG. This unpaired electron in O atoms is stabilized due to ferromagnetic exchange interaction between the O and the Fe T_d atoms, so it has the least energy when it is spin aligned

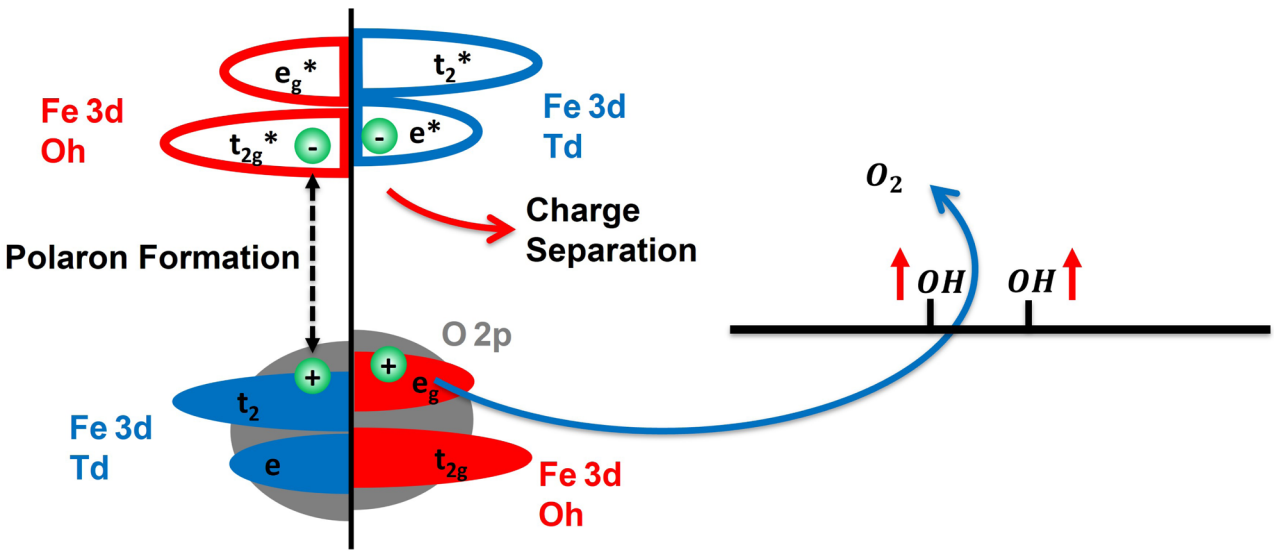

Fig. 6 Illustration of selective polaron formation and subsequent electron–hole pair recombination in O_h sites, leading to spin polarized hole accumulation at the YIG surface. These spin polarized holes represent the redox equivalents that drive spin selective water oxidation along the triplet pathway favoring the generation of O_2.

with the T_d lattice. This explains the long-lived spin polarization in the material which can persist even on the ms time scale. Together, these two new features in the Fe $M_{2,3}$ and O L_1-edges correspond to the accumulation of spin polarized holes in the surface of YIG, which are shared between hybridized O 2p and O_h Fe 3d valence band orbitals.

Based on these findings Fig. 6 summarizes the excited state spin polarized electron dynamics in YIG that give rise to spin selective photocatalytic water oxidation. Initial photoexcitation with visible light simultaneously excites both the O_h and T_d sub-lattices. Photoexcited electrons in the O_h sub-lattice rapidly trap as small electron polarons as evidenced by Fig. 1, while electrons in the T_d sub-lattice have much higher mobility and are free to exit the surface depletion region *via* drift into bulk. Because of spin selective electron trapping in the O_h sub-lattice, subsequent electron–hole pair recombination gives rise to a residual spin polarized hole population at the YIG surface. These holes reside in the hybridized valence band with shared O 2p and O_h Fe 3d character and live for greater than 1 ms allowing them to drive spin selective water oxidation at the YIG surface as shown in Fig. 6. It is this spin polarized ligand hole population that is responsible for guiding water oxidation along the triplet pathway leading to improved kinetics for O_2 production.

We note that experimental considerations necessitate the use of different samples for XUV and PEC measurements. To avoid non-resonant surface scattering, XUV-RA measurements require samples that are smooth on the scale of the XUV wavelengths, which is realized here by the epitaxial growth of YIG on GGG. However, the insulating nature of the GGG substrate precludes PEC measurements of these samples. Instead, PEC measurements employ nanoparticles of YIG and hematite drop cast on a conductive magnetic rotating disk electrode. This provides the added benefit of increasing the electrochemically active surface area of the photocatalytic samples. Despite differences in the exact sample morphology, the comparison between YIG and hematite in terms of both XUV-RA and PEC measurements, which both consist of well-characterized materials matching the specified phase and composition, form the basis for reliable conclusions regarding the origin of enhanced performance by YIG for photocatalytic water splitting.

3. Conclusion

In summary, this work provides a comparison of YIG and hematite as photoanodes for water oxidation. YIG shows nearly an order of magnitude enhancement in photocurrent density relative to hematite and a significantly enhanced yield for the production of O_2. Direct observation of surface electron dynamics using surface-sensitive XUV spectroscopy reveals that this improved performance results from reduced polaron formation efficiency in YIG relative to hematite, which gives rise to spin selective electron–hole pair recombination and spin polarized hole accumulation at the YIG surface. Surface-sensitive XUV-MCD measurements provide the first direct observation of spin polarized charge accumulation, showing that these holes are long-lived (>1 ms) and are hybridized between the O_h Fe 3d and O 2p valence band states. These spin polarized charged carriers represent the redox equivalents responsible for driving efficient water oxidation along the triplet pathway leading to O_2 generation. Together these findings provide a detailed picture of the spin selective electron dynamics responsible for significantly enhanced photocatalytic activity in YIG relative to widely studied hematite and highlight YIG as a new platform for spin selective photocatalysis. All indications suggest that these findings will be general to any ferrimagnetic semiconductor, where electron mobility and recombination rates differ between the various sub-lattices, opening the door to studies of spin polarized electron dynamics and photocatalysis in a range of magnetically ordered semiconductors.

4. Experiments and methods

4.1. Sample preparation

For the XUV-RA and XUV-MCD measurements 20 nm thick $Y_3Fe_5O_{12}$ (YIG) epitaxial thin films were grown on (111) oriented $Gd_3Ga_5O_{12}$ (GGG) substrates using the off-axis sputtering technique.[102] These samples were characterized using XRD, XRR, AFM, and magnetometric measurements (see ESI Section 1†). The Fe_2O_3 (hematite) samples were prepared by sputtering Fe metal onto SiO_2 substrate and thermally annealed in air at 520 °C for 30 min. The characterization of these samples was previously reported by Husek *et al.*[44]

4.2. XUV reflection–absorption

Extreme Ultraviolet Reflection–Absorption (XUV-RA)[44,103] spectroscopy was used to perform ground state and time-resolved measurements of small polaron formation in hematite and YIG. The samples were pumped using a 400 nm beam with an area of 1.85 mm^2 and a fluence of 7.5 mJ $pulse^{-1}$ cm^{-2} incident at the sample at 70° relative to surface normal. To produce the XUV probe beam, an 800 nm driving field mixed with a 400 nm symmetry breaking field was used for high harmonic generation in helium gas. The driving field was filtered using a thin aluminum filter, which gives a high energy cutoff of 72 eV for the XUV probe beam. The XUV probe was focused using a toroid mirror and was incident on the sample at an angle of 82° relative to the surface normal. Experiments are performed at a 1 kHz repetition rate for both pump and probe beams. The specular reflectance of the XUV probe from the sample was spectrally dispersed and imaged onto a CCD detector using a concave variable line-spaced grating. The ground state XUV-RA spectrum was calculated for all energies based on the intensity of the XUV beam reflected from the YIG or hematite sample, I_{sample}, compared to the intensity reflected from a single crystal silicon reference, $I_{reference}$, using the formula,

$$RA = -\log\left(\frac{I_{sample}}{I_{reference}}\right)$$

For time-resolved measurements, the time delay between the pump pulse and the probe pulse was controlled using a linear

stage in the pump beamline, and the absolute time delay was calibrated using the results from the hematite sample, which shows an instrument response function of approximately 80 fs. The transient signal was determined from the intensity of XUV light with the pump-on $I_{\text{pump-on}}$ and pump-off $I_{\text{pump-off}}$ conditions for all the time delays using the formula,

$$\Delta\text{OD} = -\log\left(\frac{I_{\text{pump-on}}}{I_{\text{pump-off}}}\right)$$

4.3. XUV magnetic circular dichroism

The XUV Magnetic Circular Dichroism (MCD) measurements were performed on the same beamline described above with the following modifications. The sample was pumped with the same 400 nm beam but with an area of 6.42 mm^2 and a fluence of 7.5 mJ $pulse^{-1}$ cm^{-2} incident at the sample at 82° relative to the surface normal. The XUV beam was right circularly polarized using a four Mo/B_4C multilayer mirror reflector.[104–107] The sample was magnetized by a switchable magnet with an out-of-plane magnetic field of ±300 mT. The MCD signal is given by the intensity of the right circular polarized light from the north magnetized sample I_{north} and the intensity of the right circular polarized light from the south magnetized sample I_{south} using the formula,

$$\text{MCD} = -\log\left(\frac{I_{\text{north}}}{I_{\text{south}}}\right)$$

XUV-MCD measurements were performed for both the ground (400 nm pump beam off) and excited state (400 nm pump beam on) of YIG. Because XUV measurements at near-grazing angle reflection have a probe depth less than 3 nm,[46,103,108,109] both XUV-RA and XUV-MCD spectra are surface specific, showing surface polaron formation and state-resolved surface spin accumulation, respectively.

4.4. Electrochemical catalysis

Hematite (Thermo Fisher) and YIG (Sigma Aldrich) catalyst solutions were prepared by mixing 5 mg of nanoparticle powder with 125 μL of Nafion perfluorinated resin solution (Aldrich) and 2.5 mL of a water/isopropyl alcohol (3 : 1 v/v) mixture. The catalyst solutions were sonicated for 20 min to ensure a homogeneous suspension and then immediately a 2 μL aliquot was drop-cast onto a permanent magnet (K&J Magnetics) which was used as a disk electrode. Note that the magnet disk electrode has a geometric area = 0.12 cm^2 and was polished to a mirror finish using 0.05-micron-sized alumina slurry prior to drop-casting the catalyst ink. The electrode was then dried in an oven at 70 °C for 30 min to evaporate the solvents upon which the electrode was ready for electrochemical measurements. Faradaic efficiency measurements for the oxygen evolution reaction were performed in the dark, and upon irradiation, using a rotating ring-disk electrode (RRDE-31, ALS) apparatus with a CH Instruments 750c bipotentiostat. Note, the ring electrode was platinum. To irradiate the catalyst, a CM1-FO1 UV-enhanced aluminum mirror was placed under the electrochemical cell, and a xenon arc lamp, with a power of 100 mW, was focused on the electrode surface. Electrochemical measurements were made in a 0.02 M pH 8 phosphate buffer solution, purged with Ar for 30 minutes, with the catalyst-coated permanent magnet disk and a platinum ring (ALS) as the two working electrodes. The platinum ring was electrochemically cleaned by cycling the potential between −0.03 V and 1.37 V *vs.* RHE at a scan rate of 500 mV s^{-1} for 50 cycles while the catalyst-loaded permanent magnet disk electrode was kept at an open circuit. To measure the faradaic efficiency, a linear sweep voltammogram of the catalyst-loaded permanent magnet electrode was recorded at a 10 mV s^{-1} scan rate and 1600 rpm rotation rate. The ring electrode was held at a constant potential of 0.06 V *vs.* RHE such that the oxygen produced at the disk was reduced at the ring. The faradaic efficiency, FE was calculated using the equation,

$$\text{FE} = \frac{2 \times i_{\text{ring}}}{i_{\text{disk}} \times N}$$

where i_{ring} and i_{disk} are the current densities of the ring and disk electrodes, respectively, and N is the collection efficiency. Note, N is a constant whose value depends only on the geometrical aspects of the ring disk electrode and was determined to be, 0.44, from calibration experiments using a ferri/ferrocyanide redox couple. The faradaic efficiency for each electrode was measured in the dark and under irradiation, three times to ensure that photodegradation was not occurring. Moreover, each measurement was replicated for at least three independently prepared catalyst electrodes to mitigate deviations in electrode preparation. A control experiment using the ring electrode in the dark and under illumination without any catalyst deposition confirm that photoexcitation of the ring electrode did not influence the reported faradaic efficiency measurements (see ESI Section 2†).

Data availability

All relevant data has been included in the manuscript and ESI.†

Author contributions

L. R. B. and H. G. conceived the idea and planned the experiments. J. G. and D. R., with guidance from F. Y. prepared and characterized YIG samples. M. S. developed the XUV phase retarder to enable XUV-MCD measurements. H. G. and S. L. with guidance from M. S. and L. R. B. designed and assembled the XUV-MCD spectrometer. H. G., S. B., E. H., and S. L. with guidance from L. R. B. performed XUV-RA and XUV-MCD measurements. A. V. and B. P. B. with guidance from D. H. W. performed photo-electrocatalysis measurements. H. G. and J. M. with guidance from F. M. M. G. and L. R. B. simulated XUV-MCD spectra using charge transfer multiplet theory. A. V., B. P. B., and D. H. W. analyzed photo-electrocatalysis data. H. G. and L. R. B. analyzed the XUV-RA and XUV-MCD data. H. G. and L. R. B. wrote the paper. All authors reviewed and edited the paper.

Conflicts of interest

There are no conflicts to declare.

Acknowledgements

Design, assembly, and demonstration of XUV-MCD capabilities on the existing XUV beamline, as well as growth and characterization of epitaxial YIG samples for XUV measurements, were supported by the Center for Emergent Materials, an NSF MRSEC, under award number DMR-2011876. Measurements of relative polaron formation efficiencies in YIG and hematite were supported by the United States Air Force Office of Scientific Research under AFOSR Award No. FA95550-19-1-0184. Ligand multiplet simulations of XUV-MCD spectra were supported by a Camille Dreyfus Teacher-Scholar Award to L. R. B. Electrochemical and photoelectrochemical activity and selectivity measurements were supported by United States National Science Foundation under NSF Award No. CHE-2140249 to D. H. W.

References

1 Z. Xing, X. Zong, J. Pan and L. Wang, *Chem. Eng. Sci.*, 2013, **104**, 125–146.
2 C.-H. Liao, C.-W. Huang and J. C. Wu, *Catalysts*, 2012, **2**, 490–516.
3 C. Acar, I. Dincer and G. F. Naterer, *Int. J. Energy Res.*, 2016, **40**, 1449–1473.
4 R. D. Tentu and S. Basu, *Curr. Opin. Electrochem.*, 2017, **5**, 56–62.
5 S. van Renssen, *Nat. Clim. Change*, 2020, **10**, 799–801.
6 DOE, US Department of Energy, Washington, DC, 2022.
7 M. Capdevila-Cortada, *Nat. Catal.*, 2019, **2**, 1055.
8 V. Kyriakou, I. Garagounis, A. Vourros, E. Vasileiou and M. Stoukides, *Joule*, 2020, **4**, 142–158.
9 G. Zang, P. Sun, A. Elgowainy, A. Bafana and M. Wang, *Environ. Sci. Technol.*, 2021, **55**, 3888–3897.
10 A. Rahbari, A. Shirazi, M. B. Venkataraman and J. Pye, *AIP Conf. Proc.*, 2020, 170011.
11 W. Lubitz, M. Chrysina and N. Cox, *Photosynth. Res.*, 2019, **142**, 105–125.
12 J. P. McEvoy and G. W. Brudvig, *Chem. Rev.*, 2006, **106**, 4455–4483.
13 R. Naaman, Y. Paltiel and D. H. Waldeck, *Acc. Chem. Res.*, 2020, **53**, 2659–2667.
14 R. Naaman, Y. Paltiel and D. H. Waldeck, *Annu. Rev. Biophys.*, 2022, **51**, 99–114.
15 S. F. Ozturk and D. D. Sasselov, *Proc. Natl. Acad. Sci. U. S. A.*, 2022, **119**, e2204765119.
16 B. P. Bloom, A. R. Waldeck and D. H. Waldeck, *Proc. Natl. Acad. Sci. U. S. A.*, 2022, **119**, e2210505119.
17 Y. Jiao, R. Sharpe, T. Lim, J. H. Niemantsverdriet and J. Gracia, *J. Am. Chem. Soc.*, 2017, **139**, 16604–16608.
18 D. Waldeck, R. Naaman and Y. Paltiel, *APL Mater.*, 2021, **9**, 040902.
19 K. Ghosh, W. Zhang, F. Tassinari, Y. Mastai, O. Lidor-Shalev, R. Naaman, P. Möllers, D. Nürenberg, H. Zacharias, J. Wei, *et al.*, *J. Phys. Chem. C*, 2019, **123**, 3024–3031.
20 S. Ghosh, B. P. Bloom, Y. Lu, D. Lamont and D. H. Waldeck, *J. Phys. Chem. C*, 2020, **124**, 22610–22618.
21 T. Bai, J. Ai, L. Liao, J. Luo, C. Song, Y. Duan, L. Han and S. Che, *Angew. Chem., Int. Ed.*, 2021, **60**, 9421–9426.
22 Y. Li, X. Wang, J. Miao, J. Li, X. Zhu, R. Chen, Z. Tang, R. Pan, T. He and J. Cheng, *Adv. Mater.*, 2020, **32**, 1905585.
23 W. Zhang, K. Banerjee-Ghosh, F. Tassinari and R. Naaman, *ACS Energy Lett.*, 2018, **3**, 2308–2313.
24 A. Vadakkayil, C. Clever, K. N. Kunzler, S. Tan, B. P. Bloom and D. H. Waldeck, *Nat. Commun.*, 2023, **14**, 1067.
25 H. Im, S. Ma, H. Lee, J. Park, Y. S. Park, J. Yun, J. Lee, S. Moon and J. Moon, *Energy Environ. Sci.*, 2023, **16**, 1187–1199.
26 W. Mtangi, F. Tassinari, K. Vankayala, A. Vargas Jentzsch, B. Adelizzi, A. R. Palmans, C. Fontanesi, E. Meijer and R. Naaman, *J. Am. Chem. Soc.*, 2017, **139**, 2794–2798.
27 J. Li, J. Ma, Z. Ma, E. Zhao, K. Du, J. Guo and T. Ling, *Adv. Energy Sustainability Res.*, 2021, **2**, 2100034.
28 T. Wu and Z. J. Xu, *Curr. Opin. Electrochem.*, 2021, **30**, 100804.
29 F. A. Garcés-Pineda, M. Blasco-Ahicart, D. Nieto-Castro, N. López and J. R. Galán-Mascarós, *Nat. Energy*, 2019, **4**, 519–525.
30 X. Ren, T. Wu, Y. Sun, Y. Li, G. Xian, X. Liu, C. Shen, J. Gracia, H.-J. Gao, H. Yang, *et al.*, *Nat. Commun.*, 2021, **12**, 2608.
31 T. Wu, X. Ren, Y. Sun, S. Sun, G. Xian, G. G. Scherer, A. C. Fisher, D. Mandler, J. W. Ager, A. Grimaud, *et al.*, *Nat. Commun.*, 2021, **12**, 3634.
32 R. R. Chen, Y. Sun, S. J. H. Ong, S. Xi, Y. Du, C. Liu, O. Lev and Z. J. Xu, *Adv. Mater.*, 2020, **32**, 1907976.
33 T. Lim, J. Niemantsverdriet and J. Gracia, *ChemCatChem*, 2016, **8**, 2968–2974.
34 P. V. Möllers, J. Wei, S. Salamon, M. Bartsch, H. Wende, D. H. Waldeck and H. Zacharias, *ACS Nano*, 2022, **16**, 12145–12155.
35 B. Göhler, V. Hamelbeck, T. Markus, M. Kettner, G. Hanne, Z. Vager, R. Naaman and H. Zacharias, *Science*, 2011, **331**, 894–897.
36 M. Kettner, D. K. Bhowmick, M. Bartsch, B. Göhler and H. Zacharias, *Adv. Mater. Interfaces*, 2016, **3**, 1600595.
37 P. V. Möllers, S. Ulku, D. Jayarathna, F. Tassinari, D. Nürenberg, R. Naaman, C. Achim and H. Zacharias, *Chirality*, 2021, **33**, 93–102.
38 M. Kettner, B. Gohler, H. Zacharias, D. Mishra, V. Kiran, R. Naaman, C. Fontanesi, D. H. Waldeck, S. S. ęk, J. Pawłowski, *et al.*, *J. Phys. Chem. C*, 2015, **119**, 14542–14547.
39 M. Kettner, V. V. Maslyuk, D. Nürenberg, J. Seibel, R. Gutierrez, G. Cuniberti, K.-H. Ernst and H. Zacharias, *J. Phys. Chem. Lett.*, 2018, **9**, 2025–2030.
40 J. Fransson, *Isr. J. Chem.*, 2022, e202200046.

41 L. Zhou, A. Shinde, D. Guevarra, M. H. Richter, H. S. Stein, Y. Wang, P. F. Newhouse, K. A. Persson and J. M. Gregoire, *J. Mater. Chem. A*, 2020, **8**, 4239–4243.
42 E. Pastor, J.-S. Park, L. Steier, S. Kim, M. Grätzel, J. R. Durrant, A. Walsh and A. A. Bakulin, *Nat. Commun.*, 2019, **10**, 3962.
43 C. Lohaus, A. Klein and W. Jaegermann, *Nat. Commun.*, 2018, **9**, 4309.
44 J. Husek, A. Cirri, S. Biswas and L. R. Baker, *Chem. Sci.*, 2017, **8**, 8170–8178.
45 L. M. Carneiro, S. K. Cushing, C. Liu, Y. Su, P. Yang, A. P. Alivisatos and S. R. Leone, *Nat. Mater.*, 2017, **16**, 819–825.
46 S. Biswas, S. Wallentine, S. Bandaranayake and L. R. Baker, *J. Chem. Phys.*, 2019, **151**, 104701.
47 H. Höchst, D. Zhao and D. L. Huber, *Surf. Sci.*, 1996, **352**, 998–1002.
48 T. Koide, T. Shidara, K. Ymaguchi, A. Fujimori, H. Fukutani, N. Kimizuka and S. Kimura, *Proceedings of the 11th International Conference on Vacuum Ultraviolet Radiation Physics*, 1996, pp. 275–278.
49 M. Pretorius, J. Friedrich, A. Ranck, M. Schroeder, J. Voss, V. Wedemeier, D. Spanke, D. Knabben, I. Rozhko, H. Ohldag, *et al.*, *Phys. Rev. B: Condens. Matter Mater. Phys.*, 1997, **55**, 14133.
50 N. Telling, A. Haznar, G. Van der Laan, M. Roper, F. Schedin and G. Thornton, *Phys. B*, 2004, **345**, 157–160.
51 R. Metselaar and P. Larsen, *Solid State Commun.*, 1974, **15**, 291–294.
52 A. Kumar, R. Kumar, N. Verma, A. Anupama, H. K. Choudhary, R. Philip and B. Sahoo, *Opt. Mater.*, 2020, **108**, 110163.
53 S. Mochizuki, *Phys. Status Solidi A*, 1977, **41**, 591–594.
54 C. Xia, Y. Jia, M. Tao and Q. Zhang, *Phys. Lett. A*, 2013, **377**, 1943–1947.
55 W.-K. Li and G.-Y. Guo, *Phys. Rev. B*, 2021, **103**, 014439.
56 S. Biswas, J. Husek, S. Londo and L. R. Baker, *Nano Lett.*, 2018, **18**, 1228–1233.
57 I. M. Klein, H. Liu, D. Nimlos, A. Krotz and S. K. Cushing, *J. Am. Chem. Soc.*, 2022, **144**, 12834–12841.
58 Y. Takada and M. Masaki, *J. Supercond. Novel Magn.*, 2007, **20**, 629–633.
59 M. Battiato, K. Carva and P. M. Oppeneer, *Phys. Rev. Lett.*, 2010, **105**, 027203.
60 P. Larsen and R. Metselaar, *Phys. Rev. B: Solid State*, 1976, **14**, 2520.
61 J. Costantini, F. Brisard, A. Meftah, F. Studer and M. Toulemonde, *Nucl. Instrum. Methods Phys. Res., Sect. B*, 1994, **91**, 288–293.
62 N. Thiery, V. V. Naletov, L. Vila, A. Marty, A. Brenac, J.-F. Jacquot, G. de Loubens, M. Viret, A. Anane, V. Cros, *et al.*, *Phys. Rev. B*, 2018, **97**, 064422.
63 B. Warnes, F. Aplan and G. Simkovich, *Solid State Ionics*, 1984, **12**, 271–276.
64 P. Liao and E. A. Carter, *J. Appl. Phys.*, 2012, **112**, 013701.
65 B. Deka, S. Ravi, D. Pamu, *et al.*, *Ceram. Int.*, 2017, **43**, 10468–10477.
66 H. Li, *Ceram. Int.*, 2020, **46**, 15408–15416.
67 O. Zandi and T. W. Hamann, *Phys. Chem. Chem. Phys.*, 2015, **17**, 22485–22503.
68 C. Li, Z. Luo, T. Wang and J. Gong, *Adv. Mater.*, 2018, **30**, 1707502.
69 I. S. Cho, H. S. Han, M. Logar, J. Park and X. Zheng, *Adv. Energy Mater.*, 2016, **6**, 1501840.
70 D. K. Bora, A. Braun and E. C. Constable, *Energy Environ. Sci.*, 2013, **6**, 407–425.
71 Y. Fan, Y. Lin, K. Wang, K. H. Zhang and Y. Yang, *Phys. Rev. B*, 2021, **103**, 085206.
72 V. Gatard, J. Deseure and M. Chatenet, *Curr. Opin. Electrochem.*, 2020, **23**, 96–105.
73 R. Naaman, Y. Paltiel and D. H. Waldeck, *Nat. Rev. Chem*, 2019, **3**, 250–260.
74 Z. Bian, K. Kato, T. Ogoshi, Z. Cui, B. Sa, Y. Tsutsui, S. Seki and M. Suda, *Adv. Sci.*, 2022, **9**, 2201063.
75 Y. Zhang, C. Liang, J. Wu, H. Liu, B. Zhang, Z. Jiang, S. Li and P. Xu, *ACS Appl. Energy Mater.*, 2020, **3**, 10303–10316.
76 E. Stavitski and F. M. De Groot, *Micron*, 2010, **41**, 687–694.
77 H. B. Vasili, B. Casals, R. Cichelero, F. Macià, J. Geshev, P. Gargiani, M. Valvidares, J. Herrero-Martin, E. Pellegrin, J. Fontcuberta, *et al.*, *Phys. Rev. B*, 2017, **96**, 014433.
78 S. Londo, S. Biswas, I. V. Pinchuk, A. Boyadzhiev, R. K. Kawakami and L. R. Baker, *J. Phys. Chem. C*, 2022, **126**, 2669–2678.
79 S. Londo, S. Biswas, J. Husek, I. V. Pinchuk, M. J. Newburger, A. Boyadzhiev, A. H. Trout, D. W. McComb, R. Kawakami and L. R. Baker, *J. Phys. Chem. C*, 2020, **124**, 11368–11375.
80 U. Bergmann, C. Horne, T. Collins, J. Workman and S. Cramer, *Chem. Phys. Lett.*, 1999, **302**, 119–124.
81 G. Chen, C. Wei, Y. Zhu and H. Huang, *EcoMat*, 2023, **5**, e12294.
82 H. Sun, X. Xu, Y. Song, W. Zhou and Z. Shao, *Adv. Funct. Mater.*, 2021, **31**, 2009779.
83 P. Strasser, *Acc. Chem. Res.*, 2016, **49**, 2658–2668.
84 C. Yang and A. Grimaud, *Catalysts*, 2017, **7**, 149.
85 Y. Wang, Y. Jiang, Y. Zhao, X. Ge, Q. Lu, T. Zhang, D. Xie, M. Li and Y. Bu, *Chem. Eng. J.*, 2023, **451**, 138710.
86 M. Liu, L. Y. S. Lee and K.-Y. Wong, *Handbook of Nanomaterials and Nanocomposites for Energy and Environmental Applications*, 2021, pp. 1335–1367.
87 D. A. Kuznetsov, B. Han, Y. Yu, R. R. Rao, J. Hwang, Y. Román-Leshkov and Y. Shao-Horn, *Joule*, 2018, **2**, 225–244.
88 N. Zhang and Y. Chai, *Energy Environ. Sci.*, 2021, **14**, 4647–4671.
89 S. R. Ede and Z. Luo, *J. Mater. Chem. A*, 2021, **9**, 20131–20163.
90 H. Jung, S. Choung and J. W. Han, *Nanoscale Adv.*, 2021, **3**, 6797–6826.
91 G. Assat and J.-M. Tarascon, *Nat. Energy*, 2018, **3**, 373–386.
92 W. Li, J. Shi, K. H. Zhang and J. L. MacManus-Driscoll, *Mater. Horiz.*, 2020, **7**, 2832–2859.
93 W. Li, H. Tian, L. Ma, Y. Wang, X. Liu and X. Gao, *Mater. Adv.*, 2022, **3**, 5598–5644.

94 R. L. Bouwmeester and A. Brinkman, *Rev. Phys.*, 2021, **6**, 100056.
95 C. K. Chan, H. Tüysüz, A. Braun, C. Ranjan, F. La Mantia, B. K. Miller, L. Zhang, P. A. Crozier, J. A. Haber, J. M. Gregoire, *et al.*, *Solar Energy for Fuels*, 2015, pp. 253–324.
96 J. Y. Chen, L. Dang, H. Liang, W. Bi, J. B. Gerken, S. Jin, E. E. Alp and S. S. Stahl, *J. Am. Chem. Soc.*, 2015, **137**, 15090–15093.
97 H. Xiao, H. Shin and W. A. Goddard III, *Proc. Natl. Acad. Sci. U. S. A.*, 2018, **115**, 5872–5877.
98 H. S. Ahn and A. J. Bard, *J. Am. Chem. Soc.*, 2016, **138**, 313–318.
99 F.-T. Tsai, Y.-T. Deng, C.-W. Pao, J.-L. Chen, J.-F. Lee, K.-T. Lai and W.-F. Liaw, *J. Mater. Chem. A*, 2020, **8**, 9939–9950.
100 X. Wang, J. Dai, C. Zhou, D. Guan, X. Wu, W. Zhou and Z. Shao, *ACS Mater. Lett.*, 2021, **3**, 1258–1265.
101 G. Fu, W. Li, J.-Y. Zhang, M. Li, C. Li, N. Li, Q. He, S. Xi, D. Qi, J. L. MacManus-Driscoll, *et al.*, *Small*, 2021, **17**, 2006930.
102 F. Yang and P. C. Hammel, *J. Phys. D: Appl. Phys.*, 2018, **51**, 253001.
103 A. Cirri, J. Husek, S. Biswas and L. R. Baker, *J. Phys. Chem. C*, 2017, **121**, 15861–15869.
104 H. Höchst, R. Patel and F. Middleton, *Nucl. Instrum. Methods Phys. Res., Sect. A*, 1994, **347**, 107–114.
105 F. Willems, C. Smeenk, N. Zhavoronkov, O. Kornilov, I. Radu, M. Schmidbauer, M. Hanke, C. von Korff Schmising, M. Vrakking and S. Eisebitt, *Phys. Rev. B: Condens. Matter Mater. Phys.*, 2015, **92**, 220405.
106 C. von Korff Schmising, D. Weder, T. Noll, B. Pfau, M. Hennecke, C. Strüber, I. Radu, M. Schneider, S. Staeck, C. M. Günther, *et al.*, *Rev. Sci. Instrum.*, 2017, **88**, 053903.
107 F. Siegrist, J. A. Gessner, M. Ossiander, C. Denker, Y.-P. Chang, M. C. Schröder, A. Guggenmos, Y. Cui, J. Walowski, U. Martens, *et al.*, *Nature*, 2019, **571**, 240–244.
108 S. Bandaranayake, E. Hruska, S. Londo, S. Biswas and L. R. Baker, *J. Phys. Chem. C*, 2020, **124**, 22853–22870.
109 S. Biswas and L. R. Baker, *Acc. Chem. Res.*, 2022, **55**, 893–903.